Analysing Histology Hyperspectral Images: Does Tissue Thickness Matter?

Javier Santana-Nunez[1], Laura Quintana-Quintana[1], Himar Fabelo[2,1], Samuel Ortega[3,1,4], Esther Sauras-Colón[5,6], Noèlia Gallardo-Borràs[6], Daniel Mata-Cano[6], Carlos López-Pablo[5,6], Gustavo M. Callico[1].

[1]Research Institute for Applied Microelectronics, University of Las Palmas de Gran Canaria, Spain

[2]Fundación Canaria Instituto de Investigación Sanitaria de Canarias, Spain

[3]Norwegian Institute of Food, Fisheries and Aquaculture Research (Nofima), Tromsø, Norway

[4]University of Tromsø, Tromsø, Norway

[5]Dept. of Pathology, Hospital de Tortosa Verge de la Cinta, ICS, IISPV, Tortosa, Spain.

[6]Universitat Rovira i Virgili, Tortosa, Spain.

Citation: Javier Santana-Nunez, Laura Quintana-Quintana, Himar Fabelo, et al. "Analysing histology hyperspectral images: Does tissue thickness matter?", Proc. SPIE 13006, Biomedical Spectroscopy, Microscopy, and Imaging III, 1300611 (20 Jun 2024); https://doi.org/10.1117/12.3017010

Analysing Histology Hyperspectral Images: Does Tissue Thickness Matter?

Javier Santana-Nunez[¥,*,1], Laura Quintana-Quintana[¥,*,1] , Himar Fabelo[2,1], Samuel Ortega[3,1,4], Esther Sauras-Colón[5,6], Noèlia Gallardo-Borràs[6], Daniel Mata-Cano[6], Carlos López-Pablo[5,6], Gustavo M. Callico[1].

[1]Research Institute for Applied Microelectronics, University of Las Palmas de Gran Canaria, Spain
[2]Fundación Canaria Instituto de Investigación Sanitaria de Canarias, Spain
[3]Norwegian Institute of Food, Fisheries and Aquaculture Research (Nofima), Tromsø, Norway
[4]University of Tromsø, Tromsø, Norway
[5]Dept. of Pathology, Hospital de Tortosa Verge de la Cinta, ICS, IISPV, Tortosa, Spain.
[6]Universitat Rovira i Virgili, Tortosa, Spain.
* jsnunez@iuma.ulpgc.es, lquintana@iuma.ulpgc.es
[¥] These authors contributed equally to this work and are designated as co-first authors.

ABSTRACT

Cancer is one of the leading causes of death, thereby, contributing to their quick diagnosis or treatment is of greatest importance. Nowadays, tumours are mainly diagnosed and graded histologically using biopsies. Since the images need to be sharp to distinguish biological structures, samples are thinly sliced (3-5 μm) to avoid scattering and contrast is obtained using highly absorbance dyes (e.g., Haematoxylin and Eosin (H&E)). RGB (Red-Green-Blue) cameras have been widely employed to acquire those images, while new approaches, such as Hyperspectral (HS) Imaging (HSI), have been arising to obtain a greater amount of spectral information from the samples. However, in order to have diffuse light for the HS cameras to capture it, the thickness of the sample should be bigger than the ones employed in conventional microscopy. This work aims to characterize the influence of tissue thickness of histology breast samples sectioned at 2 and 3 μm on their spectral signatures. Based on the H&E transmittance spectra peaks, HS images were segmented into three structures: stroma (eosin-stained), nuclei (haematoxylin-stained), and background (non-stained). Results show that, spatially, in 3 μm samples there are more cells imaged than in 2 μm samples. Moreover, spectrally, 3 μm samples proportionate higher spectral contrast than 2 μm samples due the greater interaction of light with tissue, denoting them as more suitable for microscopic HSI.

Keywords- Hyperspectral Imaging, Breast Cancer, Histopathological Sample Thickness, Light Tissue Interactions.

1. INTRODUCTION

Breast cancer, a disease that annually afflicts over two million people, results in the death of more than half a million individuals each year [1]. This abnormal degree of mutated cells can be started by mammary cells (primary cancer) or by infiltrated cells into the mammary tissue (secondary cancer). Since the 1980s, the increase of early cancer detection programs in wealthy countries (e.g., United Kingdom) [1] shows a decrease in mortality, while in economically developing countries (e.g., Brazil) such tendency is not noticeable (Figure 1) [1]. These trends and bifurcations illustrate the necessity of more affordable early cancer detection programs.

Medical Hyperspectral Imaging (MHSI) is a field of Hyperspectral (HS) Imaging (HSI) that complements classic imaging techniques to obtain more data using the information given by interaction between light and biological samples [2], [3], [4]. The images obtained by HSI are called HS cubes. An HS cube is a tree-dimensional (two spatial and one spectral dimension) array of values where each one represents the irradiance of a pixel on a certain wavelength. The spectral signature is the vector of all the wavelengths of a single spatial pixel. A spectral signature is unique for each substance since light is absorbed or scattered differently by each kind of molecule depending on its chemical composition. This property allows the identification and classification of different materials [5]. The MHSI applied to cancer has shown promising results on the segmentation of normal and skin [6], breast [7], [8], and ovarian [9] cancerous tissue, among others.

Currently, the ground-truth for breast cancer diagnosis and grading is the histological study of biopsy samples extracted from the lumps detected in a patient's body. Histological tumour grade is based on the degree of differentiation of the morphological features of the tissue [10]. The breast biopsy samples are usually cut in thin slices (between 3 and 5 μm [11]) and dyed using Haematoxylin-Eosin (H&E) to highlight those differences and remark nuclei and stroma, which may point to abnormal cellular development. Afterwards, they may assess the identification of different biomarkers, (e.g., estrogenic receptors, progesterone receptors, HER2+, and Ki67) which may need the study of more samples stained with different immunochemistry [10]. In recent years, a new approach consisting in coupling HS cameras to microscopes have been researched [12], [13], [14]. This way we could extract specific information just from one slide from the patient biopsy.

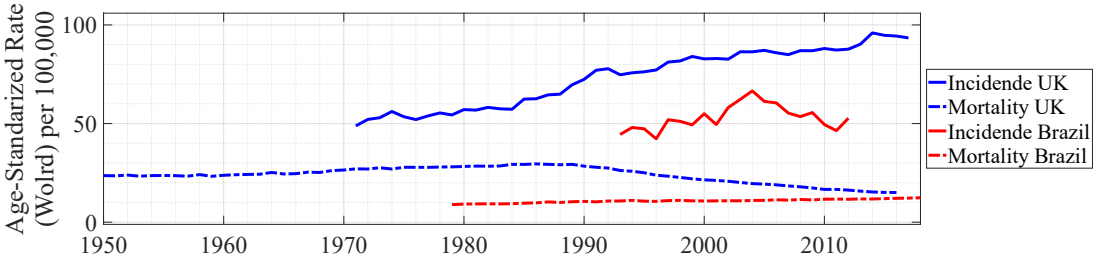

Figure 1. Incidence and Mortality evolution throughout the United Kingdom (UK) and Brazil [15].

When capturing breast biopsy samples under a RGB (Red-Green-Blue) microscope, the H&E dyes are the ones providing spatial contrast, since they absorb light in the Visible and Near Infrared (VNIR) range, from 450 to 700 nm (Figure 3c) [16]. Classic pathological approach is interested in obtaining sharp images; thus, it must reduce the scattering as much as possible. To do that the samples must be thinly sliced while maintaining the main morphological characteristics of the tissue studied [17], e.g., neurons are hundreds of thousands of times larger than red blood cells [18], so neurological biopsy samples should be sliced into thicker slides. In HS microscopy a different approach should be followed when slicing the samples since the main advantage of this technology is the capture of the diffused light obtained from the interaction of light with tissue. Following Beer-Lambert law, the thickness of the sample impacts its absorbance [19]. Since light in the VNIR range can penetrate the tissue up to 5 mm, samples should be thicker than the standard ones [20].

Previous studies have explored the influence of sample thickness on light penetration. However, these studies either used non-human samples [21], had thickness variation on the order of magnitude of the millimetres [22] (significantly higher than the traditional histology sample slide thickness and the intended thicknesses of this project), or their results were based on Monte Carlo simulations [20]. The main contribution of this work is the study of the influence of the conventional sample thicknesses over the captured diffuse light. To study it, breast samples are slices in two thicknesses (2 and 3 μm), captured with a microscopic HS system, and the spectral signatures of nuclei and stroma are analysed.

2. MATERIALS AND METHODS

2.1 Samples slides

A breast cancer biopsy from a patient was first fixed with formaldehyde and embedded into a paraffin block. Then two consecutively slides were extracted with two different thicknesses: 2 and 3 μm (Figure 2a and b). These slides were dyed using H&E and digitized using a Pannoramic 250 Flash III digital scanner (3D Histech Ltd., Budapest, Hungary). The digitized images allowed to annotate the areas where normal, Ductal Carcinoma in Situ (DCIS), or Infiltrating Ductal Carcinoma (IDC) tissue is present. The first slide has a thickness of 2 μm and contains 192 of those annotated areas, while the second slide has a thickness of 3 μm and has a larger number of annotated areas, 248 in total.

2.2 HS microscopic system and dataset

These biopsy sample slides were captured by a microscopic HS system (Figure 2c) [13], [14], [23]. This system is based on an OLYMPUS BX-53 microscope equipped with a 100 W T4Y4 Halogen Lamp from Olympus (Olympus, Tokyo, Japan) and a ×10 magnification lens (LMPLN-IR). In order to capture HS cubes, the pushbroom HS camera Hyperspec® VNIR A-Series (HeadWall Photonics, Fitchburg, MA, USA) is mounted. This camera is able to capture 826 bands within the spectral range of 400 to 1000 nm, allowing it to obtain a pixel size of 7.4 μm/pixels due to its 1004 spatial sensors. The dataset captured for this work is a set of four HS cubes of size 1004×1004×826. Due to the nature of the pushbroom camera, 1004 successive spatial lines were necessary to assemble each HS cube. The dataset is composed by two captures from the 2 μm slide and another two from the 3 μm slide, each with a field of view of 0.552 mm^2 of IDC tissue.

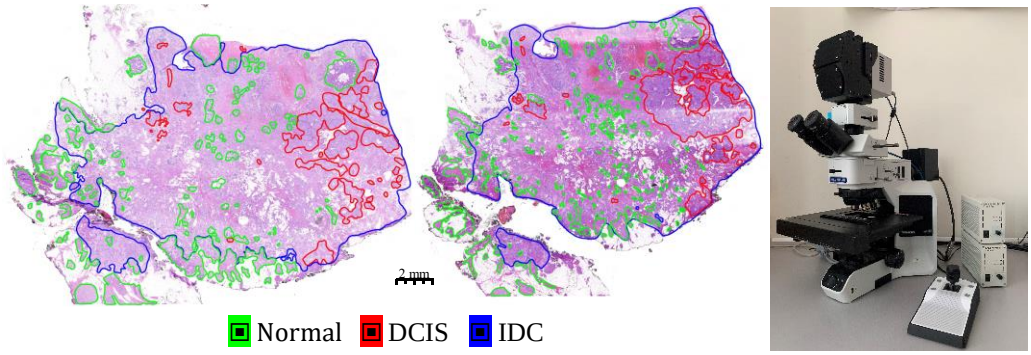

Figure 2. Materials used in this work: (a) 2 µm and (b) 3 µm biopsy slides, and (c) HS microscopic system.

2.3 Preprocessing chain

The HS cubes captured on transmittance are preprocessed in order to decrease the noise and are further manipulated to extract the absorbance and the absorption coefficient of the stroma and nuclei cellular structures. This preprocessing chain consists of: I) a flat-field correction and band reduction, II) segmentation of the cellular structures, III) filtering of outliers pixels, and IV) assembly of a synthetic RGB of each HS cube. In the following subsections, each preprocessing stage, developed using MATLAB R2022a, will be described.

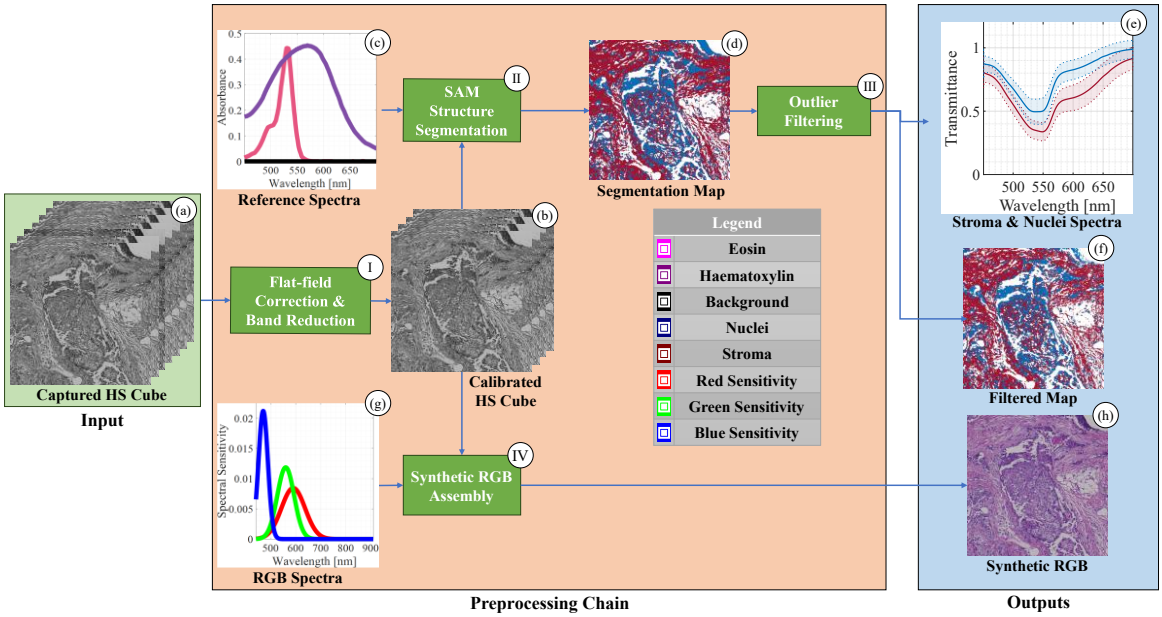

Figure 3. Preprocessing chain applied to each HS cube: (a) input HS cube, (b) calibrated HS cube, (c) absorbance reference signatures of haematoxylin, eosin, and background, (d) segmentation map, (e) stroma and nuclei filtered spectra, (f) filtered segmentation map, (g) red, green, and blue spectral sensitivity, and (h) synthetic RGB generated.

I. Flat-field correction and band reduction

The first step on the preprocessing chain is reducing the number of spectral bands of the captured HS cubes (Figure 3a). Previous works [24], [25] have shown that from the original 826 bands, only 645 bands are noise-free. From the selected bands, the H&E dyes have non-null absorbance values in the 450 to 700 nm range. So, to ensure that the signal use has the highest quality possible, the spectral range of this study has been narrowed down from 400 to 1000 nm to 450.685 to 699.516 nm (343 bands in total). Once the band reduction is performed, the flat-field correction of the remaining data is applied. In the microscopic framework used, the digital numbers reported by the camera need to be modify in order to correct the influence of the quantum efficiency and the background noise level of the sensors. The objective of the flat-field correction is to normalize the data into the 0 to 1 range, isolating the sample data from the influence of the camera

quantum efficiency, camera noise, and source light spectral non-uniformity [26]. This process consists of using a capture of the light used (*White*), a black level image (*Dark*) and a raw HS frame (*Raw*) in order to extract a calibrated HS cube (*CC*) where the transmittance values are stored.

$$CC = \frac{Raw - Dark}{White - Dark} \qquad (1)$$

II. Spectral angle mapper structure segmentation

For the first step of the proposed methodology, a segmentation between haematoxylin-dyed (nuclei) and eosin-dyed (stroma and cytoplasm) tissue is needed [27]. Since cytoplasm represents a low percentage of each cell (10 - 40% in volume) [28] and for simplification of the argument, eosin-dyed pixels will be considered stroma. Moreover, the entire sample is not dyed, e.g., ducts where there is an absence of tissue or fat which is removed during the histological process, which is reflected as white areas on the image. From now on, these areas are considered as background. Thus, three different reference spectral signatures (RS_i) for each class (C_i) are considered: haematoxylin for nuclei, eosin for stroma, and pure light for the background (Figure 3c) [29].

The Spectral Angle Mapper (SAM) metric (2) allows to define a segmentation criterion. The SAM algorithm takes as inputs a reference spectral signature and a test spectral signature (*TS*) as q -dimensional vectors and outputs the angle between them [30]. A low SAM value indicates similarity between the reference and test spectral signatures. SAM values were obtained between the CC and the three references (*haematoxylin*, *eosin*, and *background*), each pixel was assigned to the class of the minimum achieved SAM (3). The result of this segmentation process is a nuclei and stroma spectra databases, that can be represented as segmentation maps where the colour of a pixel indicates its class (Figure 3d). Background pixels would not be included in later analysis since they are the absence of tissue.

$$SAM_{TS,RS_i} = cos^{-1}\left(\frac{\sum_k^q t_k r_k}{\sqrt{\sum_k^q t_k^2}\sqrt{\sum_k^q r_k^2}}\right); r_k \in RS_i; t_k \in TS \qquad (2)$$

$$TS \in C_i : i = \underset{j}{\operatorname{argmin}}\, SAM_{TS,RS_j}, \forall\, j = \{\text{haematoxylin}, \text{eosin}, \text{background}\} \qquad (3)$$

III. Outlier filtering

In order to reduce the variability of the nuclei and stroma spectra databases, the outlier pixels of each class are removed. A pixel (*P*) is considered an outlier if, at any band (*b*) from the studied spectrum (*B*), a value deviates more than three times the standard deviation (STD) above or below the mean value of the spectrum of each class at that band ($\overline{P_b}$) (4). The outliers pixels were removed from the later analysis. When the preprocessing chain is completed, the resulting spectral signatures (Figure 3e) can be used to extract the absorbance and absorption coefficients.

$$P \in Outlier \Leftrightarrow |P_b - \overline{P_b}| > 3 \cdot STD_b \forall\, b \in B \qquad (4)$$

2.4 Results evaluation

I. Qualitative evaluation

A visual comparison between the HS cubes and the filtered segmentation maps (Figure 3f) can be done to evaluate the segmentation results qualitatively. Since not all frames from a HS cube can be displayed as an RGB image at the same time, a transformation is needed. A synthetic RGB image takes a spectral signature and simulates the sensitivities of the human eye cone cells (Figure 3g) to obtain the RGB values of each pixel [31]. With these synthetic RGB images (Figure 3h), the qualitative evaluation of the segmentation of the cellular classes can be performed.

II. Spatial difference

Once a successful segmentation has been confirmed, it is possible to evaluate the differences between the biopsy samples with thicknesses of 2 and 3 μm. As the sample thickness increases, the volume of tissue per sample is expected to increase too, and so, the number of cells per slide. This spatial difference between the several thicknesses can be obtained by calculating the nuclei to stroma pixel ratio (5) .

$$Nuclei/Stroma = \frac{\#Nuclei\ Pixels}{\#Stroma\ Pixels} \cdot 100\% \qquad (5)$$

III. Spectral difference

Until now, the values captured, preprocessed, and stored on the *CC* were transmittance values. Transmittance (*T*) represents the ratio of light that has been able to get through a sample (*I*) in relation to the light emitted (I_0). However, its main issue is its non-linearity with the optical pathlength (*Z*) (6). Beer-Lambert law [19] states that the absorbance (*A*) is linearly directly related to the molar absorptivity (ϵ), the concentration of the sample (*c*) and the optical pathlength (7). Moreover, further analysis includes the comparison of the absorption coefficient (μ_a) of the different structures. The absorption coefficient is a measure of the capacity of a medium to limit the light that can pass through, per unit of optical pathlength [32], [33] (8). These resulting absorbance and absorption coefficient values allow to determine their contrast using equation (9) [34], where *X* is the mean absorbance or absorption coefficient values of a certain class and sample thickness.

$$T = \frac{I}{I_0} = e^{-\mu_a Z} \quad (6)$$

$$A = -\log_{10} T = \epsilon c Z \quad (7)$$

$$\mu_a = -\ln T / Z \quad (8)$$

$$Contrast = \sqrt{\frac{1}{N-1}\sum_{i=1}^{N}(x_i - \bar{x})^2}, \forall x_i \in X \quad (9)$$

3. RESULTS

This section will present the results obtained following the previously exposed methodology. First, the results of the nuclei and stroma segmentation and its qualitative evaluation are shown. Then, the spatial and spectral differences between the captures of the 2 and 3 µm slides are presented.

3.1 Nuclei and stroma segmentation

First, using the dataset captured, the segmentation of nuclei, stroma, and background can be performed using the SAM metric (2) and the proposed segmentation criterion (3). In Figure 4, the synthetic RGBs, segmentation maps, and the mean and STD of spectral signatures of the nuclei and stroma pixels per capture are shown.

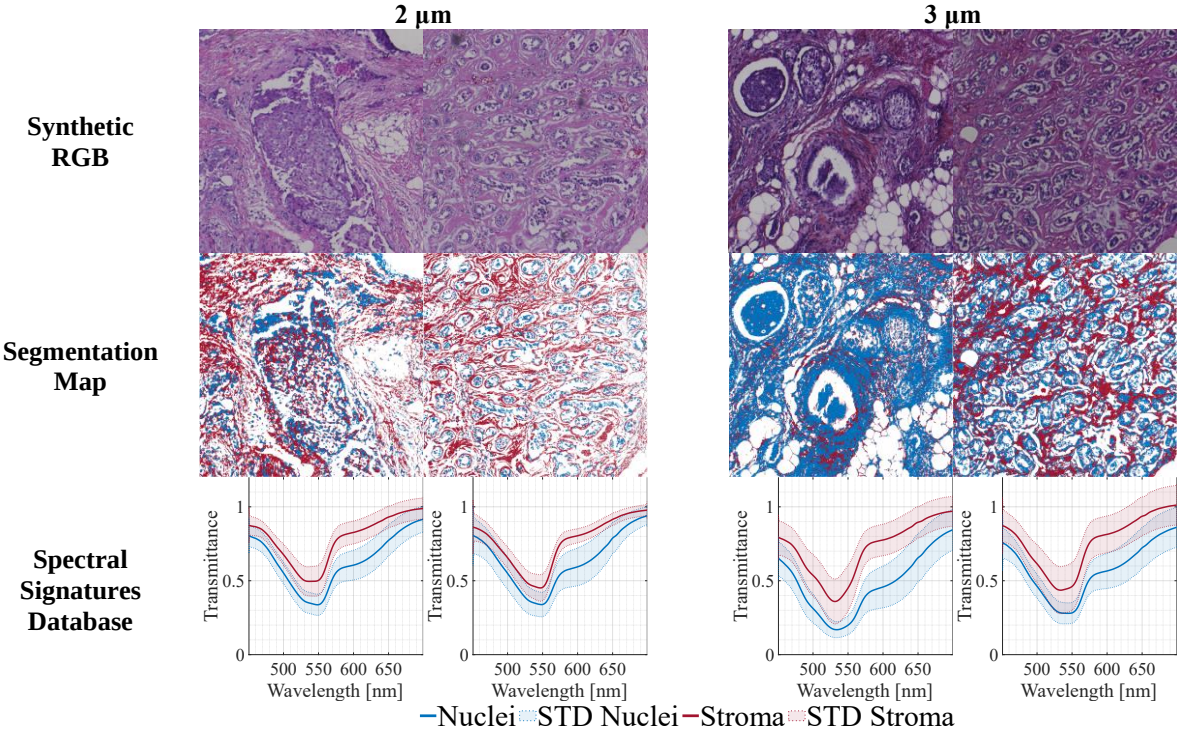

Figure 4. Synthetic RGB, Segmentation maps, and mean and STD of the spectral database of each HS cube.

3.2 Qualitative evaluation

Applying the previous segmentation maps to the synthetic RGB images, it is possible to generate a set of RGB masks where only pixels classified as nuclei or stroma are visible. Figure 5 shows that the stroma pixels are lighter than the nuclei ones, which correspond to the eosin and haematoxylin dyes, respectively (Figure 3d). This qualitative evaluation supports using H&E spectra as reference signatures to divide the HS cubes into their cellular structures.

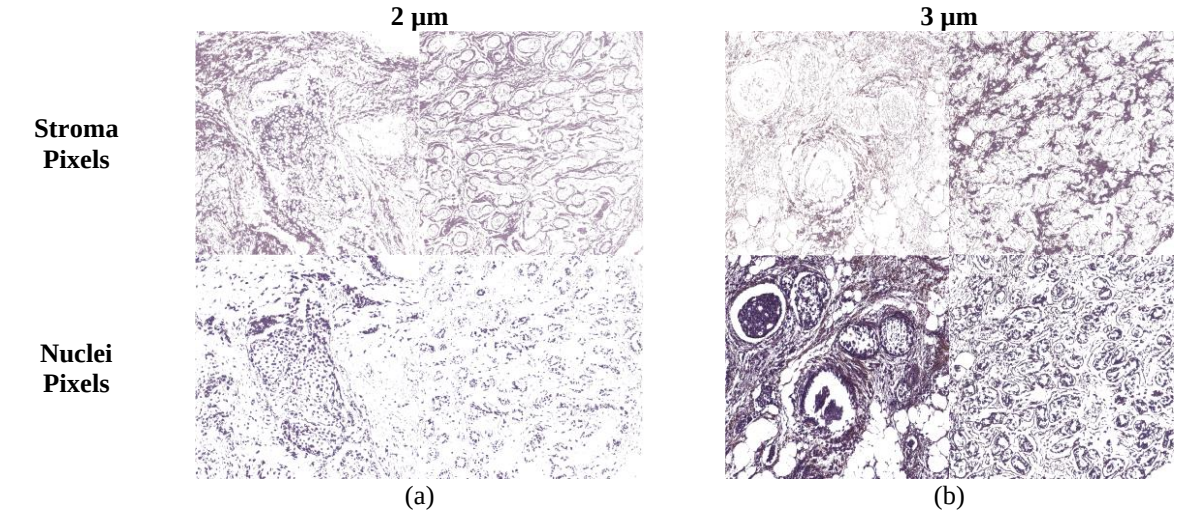

Figure 5. Stroma and Nuclei pixels on (a) 2 and (b) 3 µm HS captures.

3.3 Spatial difference

After successfully separating the stroma pixels from the nuclei pixels on each of the four images captured, we can compute the ratio of nuclei to stroma pixels. By applying equation (5) and adding up the pixel count for each class, the results shown in Figure 6 are obtained. The bar plots in Figure 6 reveal that the 2 µm captures contain fewer nuclei pixels compared to stroma pixels, with a ratio of 46.41 nuclei pixels for every 100 stroma pixels. However, the 3 µm captures exhibit a higher proportion of nuclei pixels relative to stroma pixels, with a ratio of 164.29 nuclei pixels for every 100 stroma pixels.

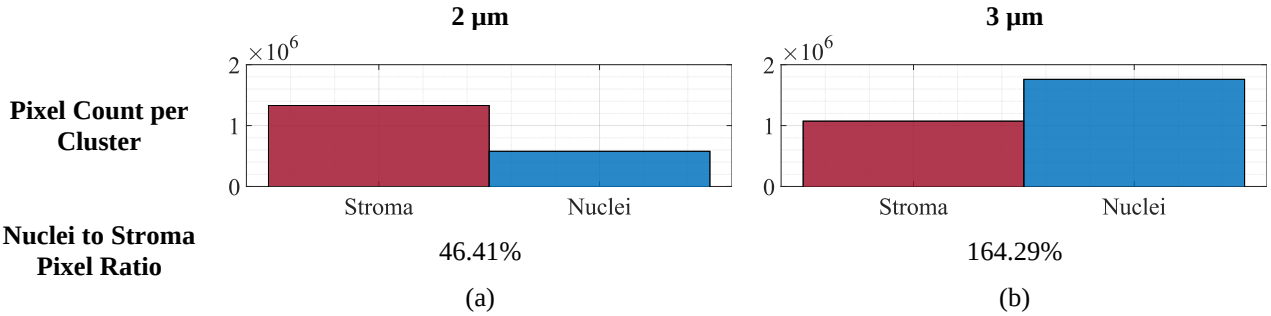

Figure 6 Count of Nuclei and Stroma pixels and ratio on (a) 2 and (b) 3 µm slides.

3.4 Spectral difference

Once the pixels corresponding to each cellular structure are identified, the absorbance and absorption coefficient of the different structures can be obtained using equation (7) and (8), respectively. A comparison between the absorbance and absorption coefficients of the different cellular structures and thicknesses is shown in Figure 7a and b, respectively. A quantitative evaluation of the contrast of each of these results is shown in Table 1 using equation (9). While the absorbance values of the 3 µm captures show a higher contrast, this effect is less appreciable on the absorption coefficient contrast values. The wider range of values of the 3 µm absorbance indicates its higher contrast between classes, making it more suitable for differentiating tissues in MHSI applications.

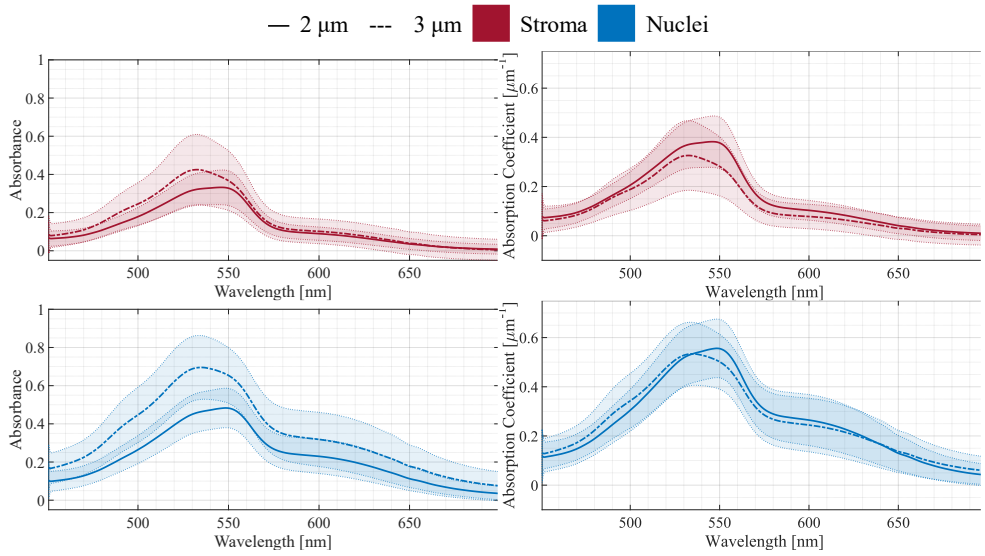

Figure 7. Mean and STD of (a) the absorbance and (b) the absorption coefficient of (top) stroma and (bottom) nuclei pixels in 2 and 3 µm slides.

Table 1 Contrast on the Absorbance and Absorption Coefficient mean values.

Cellular Structure	Thickness	Absorbance Contrast	Absorption Coefficient Contrast
Stroma	2 µm	0.1113	0.1281
	3 µm	**0.1411**	0.1083
Nuclei	2 µm	0.1523	0.1753
	3 µm	**0.2064**	0.1584

4. CONCLUSIONS

The recent decades have shown that early cancer detection programs are key to increase the survival rate. In this concern, the use of MHSI techniques in combination with microscopic systems are highly promising tools to approach histopathological diagnosis. In traditional histopathology, samples are prepared to optimize the RGB image quality based primarily on the morphological properties of the biological sample (samples are thin to enhance the clearness of the cellular structures in the visible spectrum). However, in MHSI these characteristics are key factors to obtain distinguished spectral signatures between pathological and normal tissue. As tissue thickness has been understudied for its effective selection in microscopic HS applications, this work aims to characterize its influence on histopathologic samples for microscopic HSI. A breast cancer biopsy sample was cut into 2 and 3 µm slides, dyed using H&E, and imaged to obtain four HS cubes. The nuclei and stroma pixels of each capture were segmented using the SAM metric and processed to obtain a transmittance spectra database of each cellular structure. These segmented pixels, in combination with the synthetic RGB image of each HS cube, allowed to qualitatively ensure that the pixels had been correctly categorized.

Spatially, the pixel count on each spectral database indicates how the stroma and nuclei are represented depending on the slide thickness. Results showed that the number of nuclei pixels in relation with the number of stroma pixels imaged in the 3 µm HS cubes is three times higher than in the 2 µm HS cubes, meaning that there is a higher number of cells being imaged. Spectrally, the segmented pixels allowed to obtain the absorbance values and absorption coefficients of the stroma and nuclei cellular structures. The higher contrast of the 3 µm absorbance, in comparison with the 2 µm ones, show that 3 µm samples absorb more light than 2 µm samples. This increase in the overall absorbed light with the tissue sample thickness aligns with the biphotonic literature that states that as the light pathlength increases, the probability of a photon to be absorbed is higher [33], [35]. Moreover, subtracting the influence of the tissue thickness the absorption coefficient shows that it is independent of the sample. In conclusion, the use of 3 µm biopsy sample slides is recommended over the 2 µm ones, as they show higher cell count and higher spectral contrast in the studied spectrum.

However, the main limitation of this work is the low variability on and the reduced number of the slides that have been studied, as they came from the same biopsy sample, the same type of tissue, and they were stained using the same dyes. In conclusion, these preliminary results open the discussion about the possibility of transforming the classic pathological workflow of fixing, cutting, and dyeing a biological sample, to be accommodated to use HS techniques in microscopy. Further research of other thickness is needed to stablish the optimal one for analysing histology HS images.

ACKNOWLEDGEMENT

This manuscript was developed within TALENT-HExPERIA (HypErsPEctRal Imaging for Artificial intelligence applications) project (PID2020-116417RB-C42) supported by the Spanish Government and European Union. It was completed while Javier Santana was beneficiary of the Investigo Program (Reference: 32/39/2022-0923131539) of the Canary Islands Employment Service ("Fondos del Plan de Recuperación, Transformación y Resiliencia" - Next Generation EU). Moreover, this work was developed thanks to the colaboration with the Netherlands Cancer Institute (NKI), while Laura Quintana was doing a research stay with the support of the "Consejería de Universidades, Ciencia e Innovación y Cultura" and the "Fondo Social Europeo plus". Laura Quintana was also beneficiary of the pre-doctoral grant given by the "Agencia Canaria de Investigacion, Innovacion y Sociedad de la Información (ACIISI)" of the "Consejería de Economía, Conocimiento y Empleo", which is part-financed by the European Social Fund (FSE) (POC 2014-2020, Eje 3 Tema Prioritario 74 (85%)).

REFERENCES

[1] C. Coleman, 'Early detection and screening for breast cancer', *Semin Oncol Nurs*, vol. 33, no. 2, pp. 141–155, 2017, doi: 10.1016/j.soncn.2017.02.009.

[2] G. Lu and B. Fei, 'Medical hyperspectral imaging: a review', *J Biomed Opt*, vol. 19, no. 1, p. 010901, Jan. 2014, doi: 10.1117/1.JBO.19.1.010901.

[3] B. Fei, 'Hyperspectral imaging in medical applications', *Data Handling in Science and Technology*, vol. 32, pp. 523–565, Jan. 2019, doi: 10.1016/B978-0-444-63977-6.00021-3.

[4] R. Cui *et al.*, 'Deep Learning in Medical Hyperspectral Images: A Review', *Sensors 2022, Vol. 22, Page 9790*, vol. 22, no. 24, p. 9790, Dec. 2022, doi: 10.3390/S22249790.

[5] H. Fabelo *et al.*, 'Spatio-spectral classification of hyperspectral images for brain cancer detection during surgical operations', 2018, doi: 10.1371/journal.pone.0193721.

[6] D. T. Dicker *et al.*, 'Differentiation of normal skin and melanoma using high resolution hyperspectral imaging', 2006, doi: 10.4161/cbt.5.8.3261.

[7] S. V. Panasyuk *et al.*, 'Medical hyperspectral imaging to facilitate residual tumor identification during surgery', *Cancer Biol Ther*, vol. 6, no. 3, pp. 439–446, 2007, doi: 10.4161/CBT.6.3.4018.

[8] S. Ortega *et al.*, 'Hyperspectral imaging and deep learning for the detection of breast cancer cells in digitized histological images', *Proc SPIE Int Soc Opt Eng*, vol. 11320, p. 30, Mar. 2020, doi: 10.1117/12.2548609.

[9] T. E. Renkoski, K. D. Hatch, and U. Utzinger, 'Wide-field spectral imaging of human ovary autofluorescence and oncologic diagnosis via previously collected probe data', *J Biomed Opt*, vol. 17, no. 3, p. 036003, 2012, doi: 10.1117/1.JBO.17.3.036003.

[10] E. A. Rakha *et al.*, 'Breast cancer prognostic classification in the molecular era: the role of histological grade', *Breast Cancer Res*, vol. 12, no. 4, Aug. 2010, doi: 10.1186/BCR2607.

[11] M. Veta, J. P. W. Pluim, P. J. Van Diest, and M. A. Viergever, 'Breast cancer histopathology image analysis: A review', *IEEE Trans Biomed Eng*, vol. 61, no. 5, pp. 1400–1411, 2014, doi: 10.1109/TBME.2014.2303852.

[12] S. Ortega, M. Halicek, H. Fabelo, G. M. Callico, and B. Fei, 'Hyperspectral and multispectral imaging in digital and computational pathology: a systematic review [Invited]', *Biomedical Optics Express, Vol. 11, Issue 6, pp. 3195-3233*, vol. 11, no. 6, pp. 3195–3233, Jun. 2020, doi: 10.1364/BOE.386338.

[13] S. Ortega *et al.*, 'Hyperspectral Imaging for the Detection of Glioblastoma Tumor Cells in H&E Slides Using Convolutional Neural Networks', *Sensors*, vol. 20, no. 7, p. 1911, Mar. 2020, doi: 10.3390/s20071911.

[14] S. Ortega *et al.*, 'Hyperspectral imaging and deep learning for the detection of breast cancer cells in digitized histological images', *https://doi.org/10.1117/12.2548609*, vol. 11320, pp. 206–214, Mar. 2020, doi: 10.1117/12.2548609.

[15] 'Global Cancer Observatory'. Accessed: Feb. 16, 2024. [Online]. Available: https://gco.iarc.fr/en

[16] S. L. Gibbs *et al.*, 'Near-infrared fluorescent digital pathology for the automation of disease diagnosis and biomarker assessment', *Mol Imaging*, vol. 14, no. 4, Jun. 2015, doi: 10.2310/7290.2015.00005.
[17] C. Matenaers, B. Popper, A. Rieger, R. diger Wanke, and A. Blutke, 'Practicable methods for histological section thickness measurement in quantitative stereological analyses', 2018, doi: 10.1371/journal.pone.0192879.
[18] D. B. McMillan and R. J. Harris, 'An Atlas of Comparative Vertebrate Histology', *An Atlas of Comparative Vertebrate Histology*, pp. 1–604, Jan. 2018, doi: 10.1016/C2012-0-06909-8.
[19] I. Oshina and J. Spigulis, 'Beer–Lambert law for optical tissue diagnostics: current state of the art and the main limitations', *J Biomed Opt*, vol. 26, no. 10, Oct. 2021, doi: 10.1117/1.JBO.26.10.100901.
[20] C. Ash, M. Dubec, K. Donne, and T. Bashford, 'Effect of wavelength and beam width on penetration in light-tissue interaction using computational methods', 2017, doi: 10.1007/s10103-017-2317-4.
[21] L. Kaub and C. Schmitz, 'Comparison of the Penetration Depth of 905 nm and 1064 nm Laser Light in Surface Layers of Biological Tissue Ex Vivo', *Biomedicines 2023, Vol. 11, Page 1355*, vol. 11, no. 5, p. 1355, May 2023, doi: 10.3390/BIOMEDICINES11051355.
[22] P. J. Muller and B. C. Wilson, 'An update on the penetration depth of 630 nm light in normal and malignant human brain tissue in vivo', *Phys Med Biol*, vol. 31, no. 11, p. 1295, 1986, doi: 10.1088/0031-9155/31/11/012.
[23] S. Ortega *et al.*, 'Hyperspectral Push-Broom Microscope Development and Characterization', *IEEE Access*, vol. 7, pp. 122473–122491, 2019, doi: 10.1109/ACCESS.2019.2937729.
[24] R. Leon *et al.*, 'VNIR–NIR hyperspectral imaging fusion targeting intraoperative brain cancer detection', *Scientific Reports 2021 11:1*, vol. 11, no. 1, pp. 1–12, Oct. 2021, doi: 10.1038/s41598-021-99220-0.
[25] H. Fabelo *et al.*, 'In-Vivo Hyperspectral Human Brain Image Database for Brain Cancer Detection', *IEEE Access*, vol. 7, pp. 39098–39116, 2019, doi: 10.1109/ACCESS.2019.2904788.
[26] B. Boldrini, W. Kessler, K. Rebner, and R. W. Kessler, 'Hyperspectral Imaging: A Review of Best Practice, Performance and Pitfalls for in-line and on-line Applications', *J Near Infrared Spectrosc*, vol. 20, no. 5, pp. 483–508, Oct. 2012, doi: 10.1255/JNIRS.1003.
[27] J. K. C. Chan, 'The wonderful colors of the hematoxylin-eosin stain in diagnostic surgical pathology', *Int J Surg Pathol*, vol. 22, no. 1, pp. 12–32, Feb. 2014, doi: 10.1177/1066896913517939.
[28] A. T. Molines *et al.*, 'Physical properties of the cytoplasm modulate the rates of microtubule polymerization and depolymerization', *Dev Cell*, vol. 57, no. 4, pp. 466-479.e6, Feb. 2022, doi: 10.1016/J.DEVCEL.2022.02.001.
[29] T. Biswas, H. Suzuki, M. Ishikawa, N. Kobayashi, and T. Obi, 'Generative adversarial network based digital stain conversion for generating RGB EVG stained image from hyperspectral H&E stained image', *J Biomed Opt*, vol. 28, no. 05, May 2023, doi: 10.1117/1.JBO.28.5.056501.
[30] S. Chakravarty, B. K. Paikaray, R. Mishra, and S. Dash, 'Hyperspectral Image Classification using Spectral Angle Mapper', *Proceedings of 2021 IEEE International Women in Engineering (WIE) Conference on Electrical and Computer Engineering, WIECON-ECE 2021*, pp. 87–90, 2021, doi: 10.1109/WIECON-ECE54711.2021.9829585.
[31] D. Cao and P. A. Barrionuevo, 'Chronobiology International The Journal of Biological and Medical Rhythm Research Estimating photoreceptor excitations from spectral outputs of a personal light exposure measurement device', 2014, doi: 10.3109/07420528.2014.966269.
[32] C. Hu, F. E. Muller-Karger, and R. G. Zepp, 'Absorbance, absorption coefficient, and apparent quantum yield: A comment on common ambiguity in the use of these optical concepts', *Limnol Oceanogr*, vol. 47, no. 4, pp. 1261–1267, 2002, doi: 10.4319/LO.2002.47.4.1261.
[33] M. H. Freeman, *Optics / M.H. Freeman, C. C. Hull.*, 11th ed. 2003.
[34] E. Peli, 'Contrast in complex images', *J. Opt. Soc. Am. A*, vol. 7, no. 10, 1990.
[35] E. Chlipala *et al.*, 'Optical density-based image analysis method for the evaluation of hematoxylin and eosin staining precision', *J Histotechnol*, vol. 43, no. 1, pp. 29–37, Jan. 2020, doi: 10.1080/01478885.2019.1708611.